Chemical Engineering Journal 419 (2021) 129567

Contents lists available at ScienceDirect

Chemical Engineering Journal

journal homepage: www.elsevier.com/locate/cej

Insights into active species of ultrafine iridium oxide nanoparticle electrocatalysts in hydrogen/oxygen evolution reactions

Ning Liu [a,1], Zhiyao Duan [b,*,1], Qiaoqiao Zhang [a], Jingqi Guan [a,*]

[a] Institute of Physical Chemistry, College of Chemistry, Jilin University, Changchun 130012, PR China
[b] Department of Chemistry and Oden Institute for Computational Engineering and Sciences, The University of Texas at Austin, Austin, TX 78712-1224, USA

ARTICLE INFO

Keywords:
Boron doping
Carbon nanotube
Hydrogen evolution reaction
Iridium oxide
Oxygen evolution reaction

ABSTRACT

Heteroatom doping is a potent strategy to regulate electronic structures and improve electrocatalytic performances, which has been extensively applied in fabricating carbon-based composite catalysts. Here, we report an ultrafine iridium oxide supported on boron-doped carbon nanotubes with rich defects for high-efficiency hydrogen/oxygen evolution reactions and overall water splitting at all pH values. Theoretical study shows that the excellent OER and HER activities of ultrafine IrO_2 nanoparticles can be attributed to their enhanced redox abilities comparing to those of bulk IrO_2 catalysts. Under OER conditions, the O-excessive surface of ultrafine IrO_2 nanoparticles weakens the binding strengths of oxygenated species, leading to enhanced OER activity. Under HER conditions, the surface of the IrO_2 nanoparticle will be reduced to an intermediate state between Ir oxide and Ir metal, which greatly enhances the H binding energy and thus improves HER activity (even higher than Pt(111)).

1. Introduction

The hydrogen evolution reaction (HER) and oxygen evolution reaction (OER) are the two half reactions of water splitting, by which high purity of hydrogen can be massively produced for fuel cells and chemical applications [1]. Currently, the cost of hydrogen production for electrolytic water is generally higher than that for steam methane reforming and coal gasification [2]. One of the main reasons is the lack of high-efficiency and robust electrocatalysts to drive the HER and OER, especially OER. Although the slow kinetics of HER and OER can be expedited on Pt/Rh and RuO_2/IrO_2, respectively, the fancy prices and chemical sensitivities of these noble metals restrict their wide-scale applications [3–6]. Development of high-performance electrocatalysts for HER and OER is urgently demanded for mitigating even-growing energy and environmental crisis. Moreover, development of bifunctional HER and OER electrocatalysts is the key for unitized regenerative fuel cells [7].

In the last few years, great progress has been made for the fabrication of high-efficiency transition-metal-based bifunctional HER and OER electrocatalysts for water splitting, including nitrides [8], carbides [9], phosphides [10], sulfides [11], borides [12], (oxy)hydroxides [13], and oxides [14]. However, from the view of thermodynamics, oxides are the most stable states during the OER because nitrides, carbides, phosphides, sulfides, and borides would ultimately be oxidized to the corresponding oxides in a realistic large current system [15]. Therefore, fabrication of bifunctional oxides for HER and OER is desirable and applicable [16,17]. However, although OER can be efficiently catalyzed on some oxide catalysts, there are seldom reports about efficient HER on oxide catalysts due to high Gibbs free energy (ΔG_{H^*}) for hydrogen adsorption [18].

Iridium oxide is the most stable OER catalyst in acidic media, which also shows excellent catalytic activity in various electrolytes with wide pH values [19–22]. However, it is unstable for OER in alkaline media due to the dissolution of Ir into the solutions [23]. Moreover, iridium oxide shows poor HER activity, making itself unable to be bifunctional electrocatalyst for both HER and OER [24]. Chen et al. found that the electrons transferred from the iridium-cobalt alloy core to the graphene layers can lower the ΔG_{H^*} for HER, thus improving electrocatalytic performance [25]. Chou and coworkers found that the HER activity can be improved by coordinating iridium atom with one nitrogen and three carbon atoms [26]. We found weak adsorption of H* on IrN_4C_x sites, leading to very low HER overpotential [27]. By theoretical calculations, Baek et al. found that the empty d orbitals of iridium sites can be

* Corresponding authors.
E-mail addresses: zhiyao.duan@cm.utexas.edu (Z. Duan), guanjq@jlu.edu.cn (J. Guan).
[1] These authors contributed equally to this work.

https://doi.org/10.1016/j.cej.2021.129567
Received 14 February 2021; Received in revised form 23 March 2021; Accepted 25 March 2021
Available online 31 March 2021

decreased through interacting with adjacent C/N atoms, leading to enhanced HER activity [24]. Yang et al. found that the electronic structure of iridium oxide nanoparticles on carbon cloth can be adjusted by introduction of Pt, and the optimized catalyst showed excellent bifunctional performance for both OER and HER [28]. Therefore, it is feasible in theory to catalyze HER by modulating the electronic structure of iridium oxide. Boron (2.04 eV) shows smaller electronegativity than carbon (2.55 eV) [29]. B-doping can change the electronic structure of adjacent carbon atoms and improve the charge transfer of carbon-based materials, thus boosting electrocatalytic performance.

Since iridium is a precious metal with high price, reducing the dosage while increasing catalytic activity is highly desirable [30–34]. The surface iridium atoms can be exposed over 90% by downsizing the iridium oxide nanoparticles to the level of sub-nanometer, which can be efficaciously utilized [35,36]. Compared with single Ir atoms, ultra-small iridium oxide exhibits better electrocatalytic stability due to more saturated coordination [37]. The electronic structure of highly exposed iridium atoms can be interacted with environmental electro-negative nonmetallic atoms and be regulated to be more suitable for HER and OER [38,39]. In this work, we fabricated ultra-small iridium oxide nanoparticles on B-doped CNT for efficient HER and OER, which exhibited unprecedented catalytic performance towards full water splitting at all pH values.

2. Experimental section

2.1. Preparation of catalysts

2.1.1. Synthesis of BCNT

Boron doped multiwalled carbon nanotubes were synthesized by high temperature annealing method [40]. In a typical synthesis, multi-walled carbon nanotubes were placed on the surface of boron oxide in a alundum combustion boat, which was annealed under argon atmosphere at 1300 °C for 6 h. The obtained mixture was then heated in sodium hydroxide solution at 90 °C for 2 h to wipe off remained boron oxide. After centrifugation and washing with water, the solid was dried at 80 °C for 12 h to obtain B-doped multiwalled carbon nanotubes, which was nominated as BCNT. The surface content of B is ca. 0.5 at.%.

2.1.2. Synthesis of IrO_2@BCNT

Iridium oxide supported on BCNT was prepared by low temperature annealing method. Typically, tetrairidium dodecacarbonyl was dispersed in tetrahydrofuran solution by ultrasonic processing. Then, BCNT was added into the mixture, which was further ultrasonically treated for 1 h. After removing the tetrahydrofuran solvent, the remained solid annealed in N_2 at 190 °C for 30 min. The obtained product was mildly oxidized in air at 35 °C for 48 h to obtain IrO_2@BCNT. The iridium content in the IrO_2@BCNT samples varied from 1.0 wt% to 5.0 wt%. For the 3%IrO_2@BCNT, the Ir loading is determined to be ca. 2.8 wt% by ICP-AES.

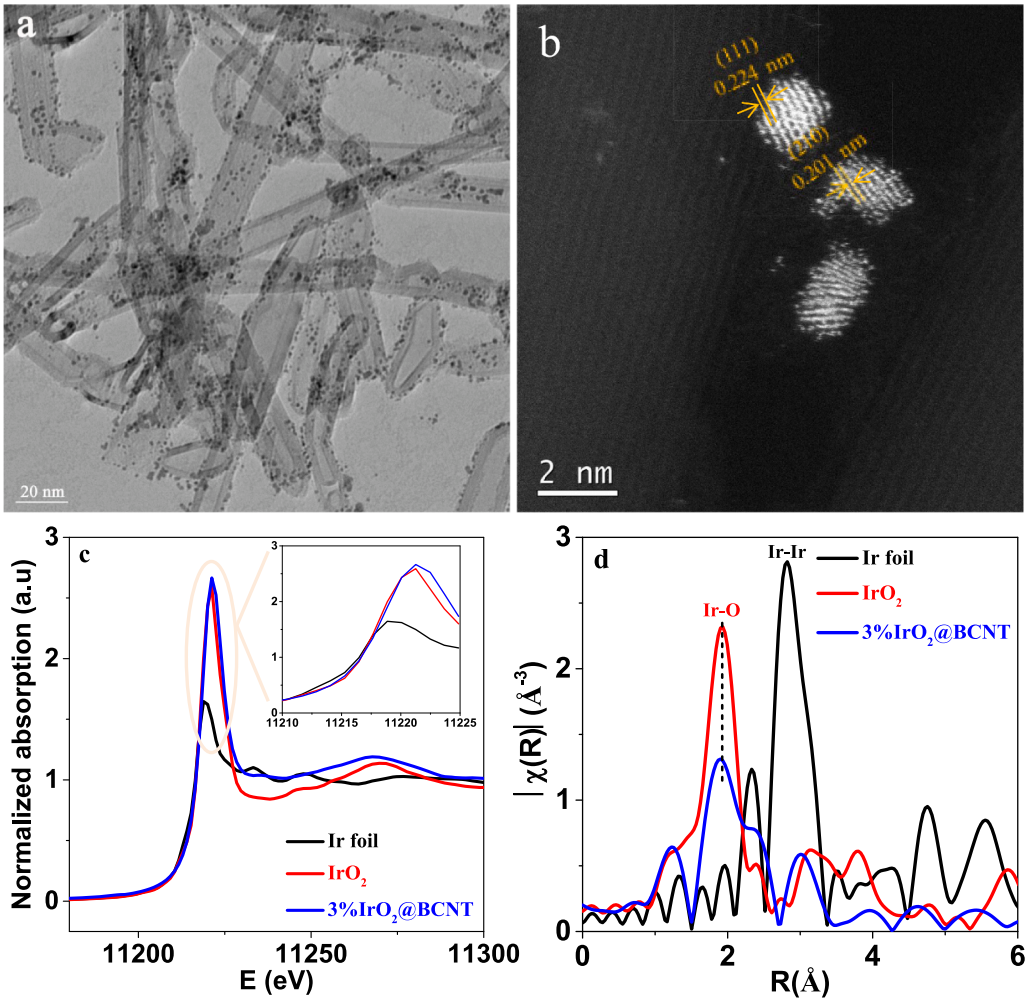

Fig. 1. (a) TEM image, and (b) HAADF-STEM image of 3%IrO_2@BCNT. (c) Ir XANES spectra, and (d) Ir EXAFS spectra of iridium foil, iridium oxide, and 3%IrO_2@BCNT.

For comparison, IrO_2@CNT with 3 wt% Ir was synthesized by a similar synthetic procedure except using CNT to replace BCNT.

3. Results and discussion

3.1. Catalyst characterization

The dispersion of iridium species on BCNT was characterized by transmission electron microscopy (TEM). As illustrated in Fig. 1a, the IrO_2 nanoparticles are well dispersed onto the BCNT with average size of 1.18 nm (Fig. S1), which are far smaller than those on pure CNT (1.56 nm), suggesting that the doping of boron into CNT favors the homogeneous dispersion of IrO_2 due to the coordination of B element with iridium species (Fig. S2). The uniform dispersion of iridium species on BCNT was further confirmed by scanning transmission electron microscopy (STEM). As depicted in Fig. S3, bright dots (Ir atoms) are homogeneously distributed onto the BCNT, further revealing good dispersion of ultrafine IrO_2 nanoparticles. The iridium species on BCNT was

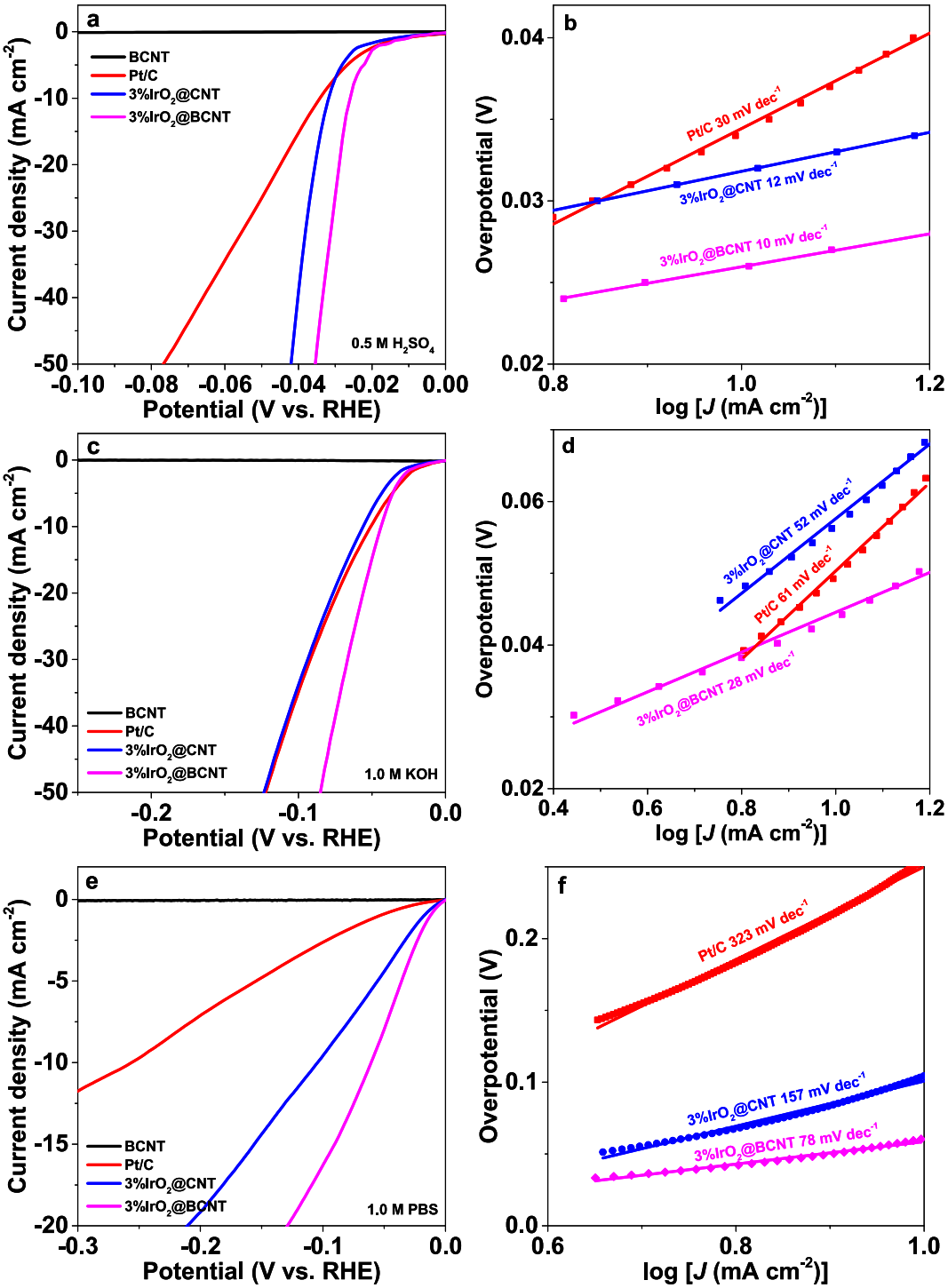

Fig. 2. (a) LSV curves of 20% Pt/C, BCNT, 3%IrO_2@CNT, and 3%IrO_2@BCNT in 0.5 M H_2SO_4. (b) The corresponding Tafel plots in H_2SO_4 solution. (c) LSV curves of 20% Pt/C, BCNT, 3%IrO_2@CNT, and 3%IrO_2@BCNT in 1 M KOH. (d) The corresponding Tafel plots in KOH solution. (e) LSV curves of 20% Pt/C, BCNT, 3% IrO_2@CNT, and 3%IrO_2@BCNT in 1 M PBS (pH = 7). (f) The corresponding Tafel plots in PBS solution.

identified by aberration corrected high-angle annular dark-field scanning transmission electron microscopy (HAADF–STEM). As shown in Fig. 1b, the distance between two adjacent lattice fringes is 0.224 and 0.201 nm, which is attributed to the (200) and (210) crystal plane of IrO_2 (PDF#15–0870), respectively, suggesting that the iridium species were completely oxidized to Ir^{IV}.

The valence state and coordination environment of iridium was analyzed by X-ray absorption fine structure (XAFS). Fig. 1c and 1d show the iridium L_3-edge X-Ray absorption near-edge structure (XANES) spectra and extended X-ray absorption fine structure (EXAFS) spectra of 3%IrO_2@BCNT, Ir foil, and IrO_2. The relative intensity of the white-line peak of 3%IrO_2@BCNT is very near to that of IrO_2 and much higher than that of Ir foil, indicating that the valence state of iridium in the 3% IrO_2@BCNT is Ir^{IV} in agreement with the HAADF-STEM result [41]. The distance of the first Ir-O/B coordination shell derived from Ir L_3-edge EXAFS spectra is 0.202 nm, longer than that of IrO_2 (0.198 nm) [42], suggesting that the doped boron should interact with the supporting IrO_2 and thus influence the electronic structure. In addition, the fitting results show that the coordination number of the Ir-O/B path is 7.0, higher than that in IrO_2 (6.0) [42]. Moreover, the absence of peaks at around 0.281 nm (corresponding to Ir-Ir path) in the EXAFS spectrum of 3%IrO_2@BCNT suggests that no metal Ir species are presented and all iridium atoms were oxidized to Ir^{IV}.

The chemical valence of iridium in 3%IrO_2@BCNT was further confirmed by X-ray photoelectron spectroscopy (XPS). As exhibited in Fig. S4, the peaks of Ir $4f_{5/2}$ and Ir $4f_{7/2}$ are centered at 64.4 and 61.5 eV, respectively, implying the presence of dominant Ir^{IV} in the sample in alignment with the HAADF-STEM and XANES results [43]. In addition, the fitting results of B 1 s show that there are BC_3 (63.3%), BC_2O (22.9%), and BCO_2 (13.8%) species [40]. For BCNT, the doping concentration of B is ca. 0.5%. The B-doping into CNT would introduce many defects due to different coordination numbers of B and C. As depicted in Fig. S5, the D band and G band in the Raman spectra are located at 1343 cm^{-1} and 1575 cm^{-1}, respectively. The I_D/I_G value for 3%IrO_2@CNT is 0.24, far lower than that (0.52) for 3%IrO_2@BCNT, indicating that more defects are presented in the latter. The defects around B sites can capture high-energy iridium species and stabilize them, resulting in better dispersion and smaller particle size of iridium species onto the BCNT than those on CNT.

3.2. HER performance

The electrocatalytic HER activity of the IrO_2@BCNT at various pH values was assessed using a typical three electrode configuration. For comparison, the electrocatalytic activity of BCNT, 3%IrO_2@CNT, and commercial 20 wt% Pt/C was also measured. First, the HER activity was evaluated in acidic medium (0.5 M H_2SO_4). As demonstrated in Fig. 2a, the polarization curve of 3%IrO_2@CNT shows a notably small onset HER overpotential close to 0 V, which can be compared with the state of the art Pt/C catalyst. However, the cathodic current increase on 3% IrO_2@BCNT is much faster than that on Pt/C when more negative potential is applied. As a result, 3%IrO_2@BCNT shows a much smaller Tafel slope (only 10 mV/decade) than the Pt/C (30 mV/decade) (Fig. 2b). Moreover, the overpotentials at 10 and 50 mA cm^{-2} for 3% IrO_2@BCNT are only 26 and 36 mV, respectively, much lower than those for 3%IrO_2@CNT (32 and 43 mV) and Pt/C (35 and 77 mV). The electrocatalytic HER activity of 3%IrO_2@BCNT can be comparable to the best HER catalysts for acidic media (Table S1). It is evident that pure BCNT exhibits very poor HER activity, which cannot deliver the current density of 10 mA cm^{-2} even at an overpotential of 300 mV, implying lack of efficient active sites for HER. The significantly improved HER activity on 3%IrO_2@BCNT suggests that the active sites for HER should be the Ir-based species.

Next, the HER activity of the IrO_2@BCNT was evaluated in basic medium (1.0 M KOH). From the HER polarization curves in Fig. 2c, it can be observed that the pristine BCNT exhibits poor HER activity, which delivers a current density of 10 mA cm^{-2} at a very high overpotential of 700 mV. When supporting ultrafine iridium oxide nanoparticles, the 3%IrO_2@BCNT displays superior HER activity with an onset potential of 11 mV (@0.5 mA cm^{-2}) and delivers a current density of 10 mA cm^{-2} at a very small overpotential of 44 mV. The enhanced HER activity of 3%IrO_2@BCNT should be mainly ascribed to the supported iridium oxide sites. As a contrast, 3%IrO_2@CNT demonstrates inferior HER activity and the onset potential and overpotential at a current density of 10 mA cm^{-2} are 15 and 56 mV, respectively, which are close to those obtained on Pt/C (10 and 51 mV), making 3% IrO_2@BCNT among the most active HER electrocatalysts for basic media (Table S2). The improved HER performance of IrO_2 supported on B-doped CNT suggests the positive role of boron. Remarkably, the Tafel slope of the 3%IrO_2@BCNT is as low as 28 mV/decade (Fig. 2d), smaller than that of 3%IrO_2@CNT (52 mV/decade) and Pt/C (61 mV/decade), indicating different HER mechanisms. On the former, the Tafel step might be predominant, while on the latter, the HER should follow the Volmer–Heyrovsky mechanism [44,45].

Finally, the HER activity of the IrO_2@BCNT was evaluated in neutral phosphate buffer solution (1 M PBS, pH = 7). Interestingly, the 3% IrO_2@BCNT shows an onset potential close to the thermodynamic potential of HER (i.e., 0 V) in the neutral medium (Fig. 2e), which surpasses most HER electrocatalysts [3]. The cathodic current of the 3% IrO_2@BCNT raises more promptly than Pt/C and 3%IrO_2@CNT as more negative potential is given. To deliver the current density of 10 mA cm^{-2}, the 3%IrO_2@BCNT needs an overpotential of only 61 mV, much smaller than Pt/C (256 mV) and 3%IrO_2@CNT (105 mV). The excellent HER activity of 3%IrO_2@BCNT can be reflected by its small Tafel slope (only 78 mV/decade) (Fig. 2f), far lower than that for Pt/C (323 mV/decade) and 3%IrO_2@CNT (157 mV/decade), which indicates that the HER on 3%IrO_2@BCNT could follow the Volmer–Heyrovsky mechanism in the neutral medium.

The effect of iridium content on the electrochemical HER performance was also investigated at various pH values. Generally, the electrocatalytic activity increases with increasing the Ir loadings. As depicted in Fig. S6, to deliver the current density of 10 mA cm^{-2} in 0.5 M H_2SO_4, 1%IrO_2@BCNT, 2%IrO_2@BCNT, 3%IrO_2@BCNT, 4% IrO_2@BCNT, and 5%IrO_2@BCNT require overpotentials of 30, 27, 26, 23, and 21 mV, respectively. The corresponding Tafel slope is 16, 12, 10, 10, and 10 mV/decade, respectively, indicating favorable HER kinetics. Moreover, in 1 M KOH, 1%IrO_2@BCNT, 2%IrO_2@BCNT, 3% IrO_2@BCNT, 4%IrO_2@BCNT, and 5%IrO_2@BCNT require overpotentials of 88, 70, 44, 40, and 38 mV to reach the current density of 10 mA cm^{-2}, respectively (Fig. S7). The corresponding Tafel slope is 97, 60, 28, 22, and 20 mV/decade, respectively, reflecting different HER mechanisms on IrO_2@BCNT with low iridium content (i.e. 1% and 2%) and IrO_2@BCNT with relatively high iridium content (i.e. 3%-5%). Furthermore, in 1 M PBS (Fig. S8), 1%IrO_2@BCNT, 2%IrO_2@BCNT, 3% IrO_2@BCNT, 4%IrO_2@BCNT, and 5%IrO_2@BCNT require overpotentials of 99, 71, 61, 53, and 47 mV to reach the current density of 10 mA cm^{-2}, respectively, demonstrating that all IrO_2@BCNT samples can efficiently catalyze HER in the neutral media. The corresponding Tafel slope is 135, 95, 78, 63, and 55 mV/decade, respectively. The enhanced HER activity with raising Ir content strongly support that the efficient active sites for HER on the IrO_2@BCNT catalysts should be iridium-based species. The electrocatalytic stability of 3%IrO_2@BCNT for HER was evaluated under acidic, basic, and neutral media. As exhibited in Fig. S9, the 3%IrO_2@BCNT can retain the electrocatalytic activity for 20 h under different media, implying promising potential for practical applications.

3.3. OER performance

The electrocatalytic OER performance of IrO_2@BCNT is studied by using a traditional three-electrode system at various pH values. For comparison, commercial IrO_2 is also measured under the same

conditions. The OER activity was first evaluated in 0.5 M H_2SO_4. As illustrated in Fig. 3a, the 3%IrO_2@BCNT exhibits outstanding OER activity with an onset overpotential of only 220 mV at a current density of 0.5 mA cm^{-2}, much lower than that for commercial IrO_2 (244 mV). To achieve the current density of 10 mA cm^{-2}, the 3%IrO_2@BCNT requires an overpotential of only 291 mV, lower than that on IrO_2 (313 mV) and 3%IrO_2@CNT (303 mV). The Tafel slope for IrO_2, 3%IrO_2@CNT, and 3%IrO_2@BCNT is 58, 53, and 52 mV/decade, respectively (Fig. 3b), indicating the rate-determining step for OER following the first electron transfer [46].

The OER activity was further assessed in 1 M KOH. From Fig. 3c, we can obviously observe that the 3%IrO_2@BCNT (only 188 mV @ 0.5 mA cm^{-2}) exhibits much lower onset overpotential than IrO_2 (208 mV) and 3%IrO_2@CNT (208 mV). To reach the current density of 10 mA cm^{-2}, the 3%IrO_2@BCNT requires an overpotential of only 242 mV, much smaller than that on IrO_2 (270 mV) and 3%IrO_2@CNT (260 mV), making 3%IrO_2@BCNT catalyst among one of the best OER electrocatalysts in alkaline media (Table S3). The excellent OER performance of 3%

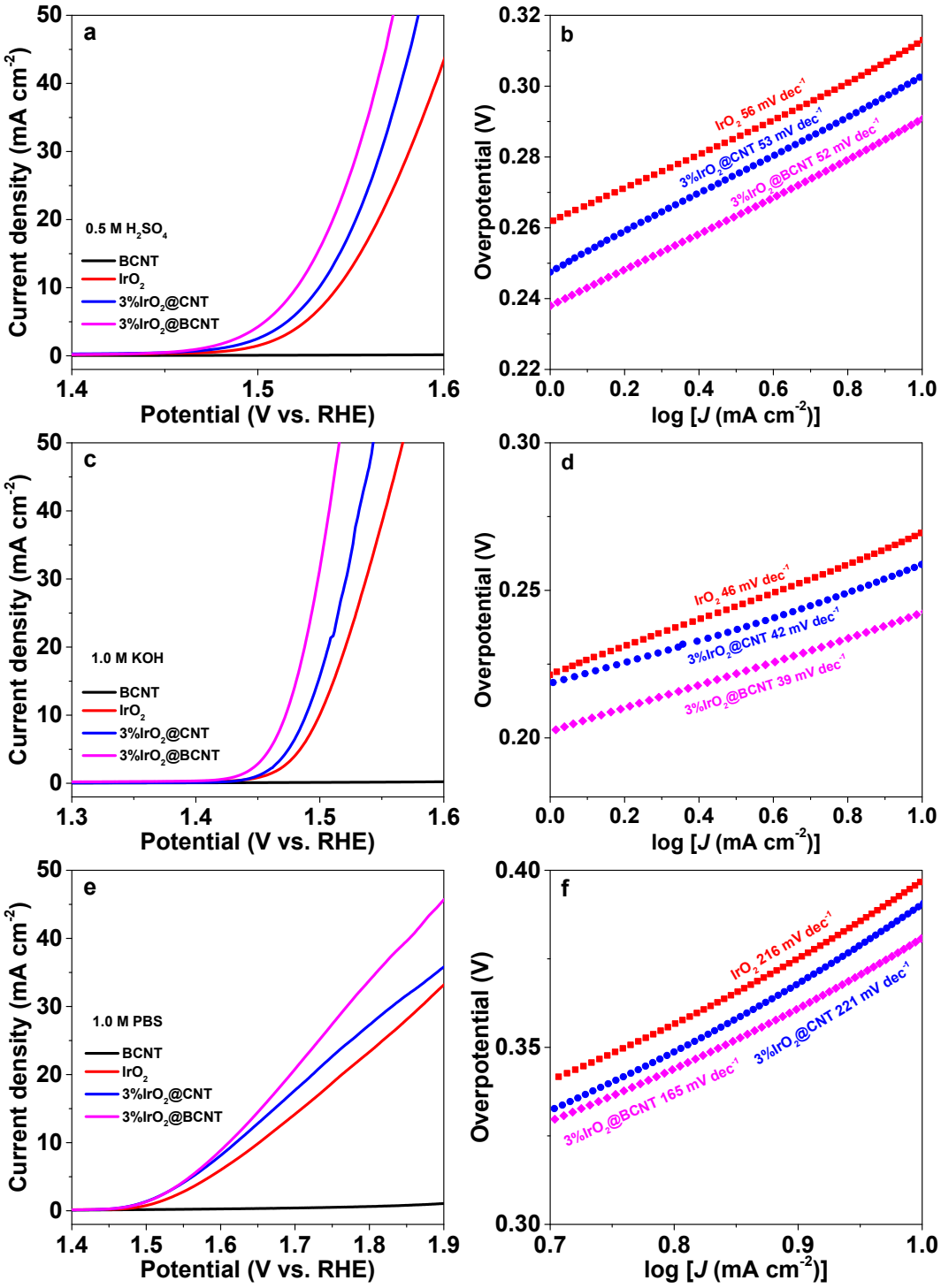

Fig. 3. (a) LSV curves of commercial IrO_2, BCNT, 3%IrO_2@CNT, and 3%IrO_2@BCNT in 0.5 M H_2SO_4. (b) The corresponding Tafel plots in H_2SO_4 solution. (c) LSV curves of commercial IrO_2, BCNT, 3%IrO_2@CNT, and 3%IrO_2@BCNT in 0.5 M H_2SO_4 in 1 M KOH. (d) The corresponding Tafel plots in KOH solution. (e) LSV curves of commercial IrO_2, BCNT, 3%IrO_2@CNT, and 3%IrO_2@BCNT in 0.5 M H_2SO_4 in 1 M PBS (pH = 7). (f) The corresponding Tafel plots in PBS solution.

IrO_2@BCNT can be reflected by its small Tafel slope (39 mV/decade), lower than that for IrO_2 (42 mV/decade) and 3%IrO_2@CNT (46 mV/decade) (Fig. 3d). The Tafel slope of these Ir-based catalysts is close to 40 mV/decade, implying that the second electron transfer is rate determining step for OER in alkaline media [46].

The catalytic activities of the as-obtained electrocatalysts for OER were finally evaluated in 1 M PBS. As displayed in Fig. 3e, the polarization curve of the 3%IrO_2@BCNT exhibits a small overpotential of 382 mV at the current density of 10 mA cm^{-2}, less than that for IrO_2 (422 mV) and 3%IrO_2@CNT (391 mV). Furthermore, the 3%IrO_2@BCNT (165 mV/decade) shows a smaller Tafel slope than IrO_2 (216 mV/decade) and 3%IrO_2@CNT (221 mV/decade) (Fig. 3f), suggesting faster increase in current by applying higher potentials for the former.

The influence of iridium content in the IrO_2@BCNT on the electrochemical OER performance was studied. As shown in Figs. S10–S12, the OER activity is improved with increasing the iridium loadings in all media, suggesting that the iridium oxide should be the active species for OER. Meanwhile, the Tafel slope decreases with raising the iridium loadings, indicating more favorable OER kinetics on IrO_2@BCNT with higher iridium content.

The OER stability in various media was evaluated. As shown in Fig. S13, the chronoamperometric responses for the 3%IrO_2@BCNT catalyst exhibit a negligible degradation of the limiting current density, suggesting superior durability of the electrocatalyst in acidic, neutral, and alkaline media. The 3%IrO_2@BCNT catalyst after HER and OER tests was characterized by XPS. As displayed in Fig. S14, there are a small quantity of iridium with low valence on the surface after HER, suggesting partial reduction of Ir^{4+} by substitution of surface O atoms by H atoms. Meanwhile, Ir^{5+} is presented on the surface of the 3% IrO_2@BCNT after OER, implying partial oxidation of Ir^{4+} to higher valence state during the oxygen evolution process [43].

3.4. Overall water splitting performance

Due to excellent bifunctional HER and OER performances, the 3% IrO_2@BCNT was assembled as the anode and cathode in a two-electrode system for electrocatalytic overall water splitting. As demonstrated in Fig. 4, the 3%IrO_2@BCNT3%IrO_2@BCNT water electrolysis device requires potentials of 1.517, 1.513, and 1.591 V vs RHE to achieve the current density of 10 mA cm^{-2} in 0.5 M H_2SO_4, 1 M KOH, and 1 M PBS, respectively, which surpass the most part bifunctional electrocatalysts (Table S4). Moreover, the bifunctional 3%IrO_2@BCNT catalyst shows robust overall water splitting performance with slight decrease in current density after operation for 12 h in all acidic, neutral, and alkaline media. No obvious Ir can be detected in the acidic and neutral media, while less than 0.1% of initial Ir was dissolved in the alkaline medium after the stability tests.

3.5. Theoretical calculations

We employed first-principles calculations to resolve the active sites responsible for the observed exceptional OER and HER activities on the ultrafine IrO_2 nanoparticles. The atomic models for the IrO_2 nanoparticle are built using Wulff construction method. We considered four different low index crystal surfaces of different surface energies, which are (1 1 0), (1 0 1), (1 0 0), and (0 0 1) surfaces with surface energies of 1.38, 1.62, 1.85, and 2.31 J/m^2, respectively [47]. The generated Wulff geometry of the rutile IrO_2 is shown in Fig. 5a. It can be seen that the nanoparticle is mostly covered by (1 1 0) and (1 0 1) surfaces, and there is also a minor coverage of the (1 0 0) surface. The atomic structure was built by cutting out an IrO_2 nanoparticle from the rutile IrO_2 bulk structure using the Wulff shape as mould. The IrO_2 nanoparticle has three O-Ir-O layers in the [1 1 0] direction, which gives a diameter of 0.6 nm for the girth and a length of 1.2 nm from top to bottom, close to the observation from electron microscope images. The surface termination of the IrO_2 nanoparticle needs to be determined. We constructed surface Pourbaix diagrams for (1 1 0) and (1 0 1) surfaces to identify stable surface structures as a function of potential and pH. As shown in Fig. S15, at OER-relevant applied potential U ~ 1.6 V_{RHE}, both surfaces should be covered with adsorbed O*. Accordingly, we capped surface Ir atoms in the IrO_2 nanoparticle with oxygen atoms, thus all Ir atoms are saturated with six O ligands. The end-up atomic structure is shown in Fig. 5a. On the surface of the IrO_2 nanoparticle, we identified eight inequivalent active sites as highlighted and indexed by numbered yellow circles. Before we start to investigate the OER activities of these active sites, the OER activities of (1 1 0) and (1 0 1) surfaces are firstly studied as references.

The free energy diagrams of OER on (1 1 0) and (1 0 1) surfaces can be seen in Fig. S16. The onset potentials for OER for (1 1 0) and (1 0 1) surfaces are 1.57 V_{RHE} (η^{OER} = 0.34 V) and 1.54 V_{RHE} (η^{OER} = 0.31 V), respectively. For IrO_2(1 1 0), the potential limiting step is the OOH* deprotonation and desorption step. For IrO_2(1 0 1) surface, the potential limiting step is the OOH* formation step. On both surfaces, the overpotentials can be further lowered if the binding strengths of adsorbates are weakened. To further demonstrate the direction of improving OER activity of IrO_2 catalysts, we constructed the volcano plot as a function of activity descriptors $\Delta G_O - \Delta G_{OH}$ and ΔG_{OH} as shown in Fig. 5b. It should be noted that we used the scaling rule $\Delta E_{OOH} = \Delta E_{OH} + 2.8$ eV, which is a better fit to the adsorption energies collected on IrO_2 surfaces and nanoparticles as shown in Fig. S17. The volcano plot confirms that

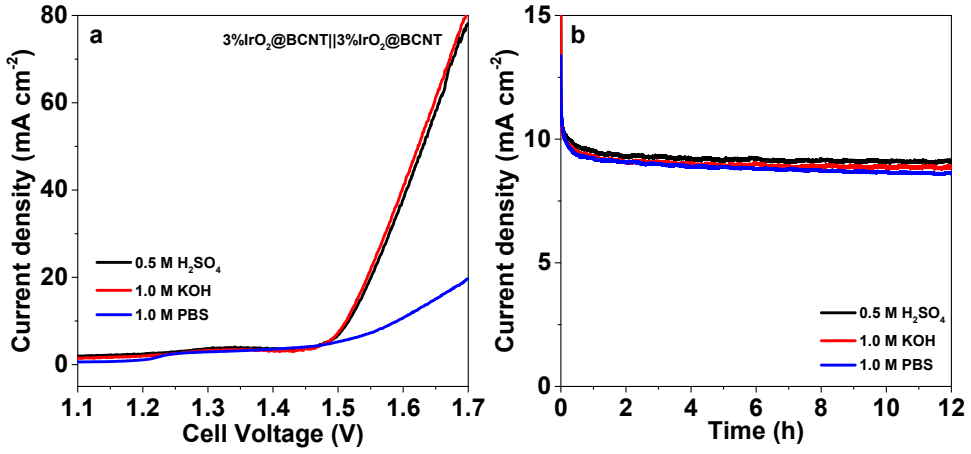

Fig. 4. (a) LSV curves of overall water splitting using 3%IrO_2@BCNT3%IrO_2@BCNT as bifunctional electrocatalysts in 0.5 M H_2SO_4, 1.0 M KOH, and 1 M PBS. (b) Chronoamperometry tests of the bifunctional overall water splitting systems in 0.5 M H_2SO_4, 1.0 M KOH, and 1 M PBS.

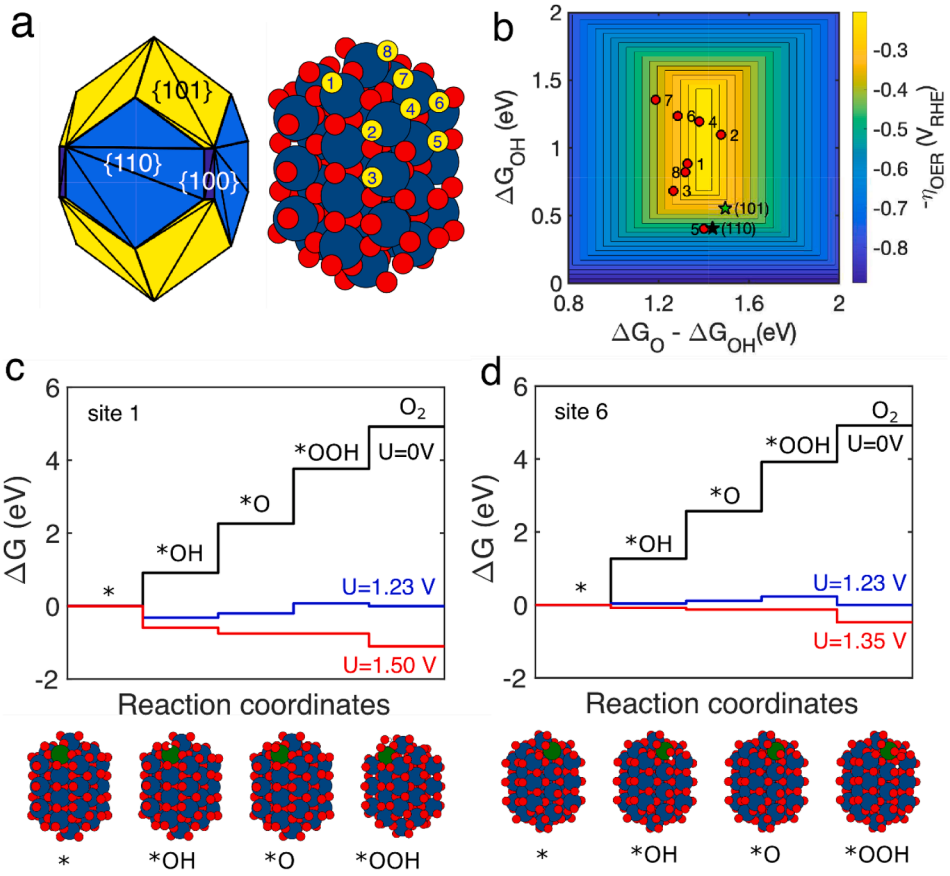

Fig. 5. (a) Geometry and atomic structure of IrO_2 nanoparticle built by Wulff construction. All eight inequivalent active sites are denoted on the atomic model. (b) Volcano plot showing the OER activity as a function of two descriptors: ΔG_O–ΔG_{OH} and ΔG_{OH}. (c,d) Free energy diagrams of OER at various applied potentials over active site 1 and site 6 on the IrO_2 nanoparticle. The atomic structures of adsorbed O*, OH*, and OOH* are shown. The Ir atoms at the active sites are colored green.

decreasing ΔG_O–ΔG_{OH} and increasing ΔG_{OH} could further enhance the OER activities of the IrO_2 surfaces. We also located various active sites of the IrO_2 nanoparticle on the volcano plot. Most of the nanoparticle active sites have decreased ΔG_O –ΔG_{OH} and increased ΔG_{OH} and some of them have nearly optimal ΔG_O–ΔG_{OH} and ΔG_{OH} with optimal OER activity according to the volcano plot. The variation of binding energies of the oxygenated species across the IrO_2 extended surfaces and various sites on the IrO_2 nanoparticle can be related to the Bader charge of the Ir atom at the vacant active site. There exists a linear relationship between binding energies and the Bader charge of the catalyzing Ir atom as shown in Fig. S18, namely more Bader electrons the Ir atom has lower binding energies are. The active sites on the IrO_2 (1 1 0) and (1 0 1) surfaces have more electrons than most active sites on the IrO_2 nanoparticle since the nanoparticle is O-rich as compared to stoichiometric IrO_2 crystal. In our oxidized IrO_2 nanoparticle model, we have 33 Ir atoms and 104O atoms, which results in an O:Ir ratio of 3.15, much larger than that of the rutile IrO_2. This structure is consistent with the aforementioned EXAFS results that the Ir-O/B coordination number in 3%IrO_2@BCNT is higher than that in bulk IrO_2. Hence, the over-oxidized nature of the IrO_2 nanoparticle leads to favorable weaker binding energies with enhanced OER activity. Specifically, we identified active sites 1 and 6 have enhanced OER activities by constructing their free energy diagrams as shown in Fig. 5c and d, respectively. The onset potentials for OER for active site 1 and 6 are 1.50 V_{RHE} (η^{OER} = 0.27 V) and 1.35 V_{RHE} (η^{OER} = 0.12 V), respectively.

Regarding HER reaction, we first understand the surface state of IrO_2 surface under HER conditions via the Pourbaix diagram shown in Fig. S15. Under HER conditions, the surface O atoms have been reduced to water and leave the surface. Meanwhile, H atoms start to adsorb on the surface as a result of H^+ reduction. At U_{RHE} = 0 V, H atoms are adsorbed on the bridging O vacancies and atop Ir sites. We add an additional H to the surface and the adsorption turns out to be too weak, leading to poor HER activity as shown in Fig. 6. We translate the surface states of IrO_2 surfaces under HER conditions to IrO_2 nanoparticle. Accordingly, we replaced all the surface O atoms with adsorbed H atoms, which is also supported by the aforementioned XPS results identifying low valence Ir ions in the 3%IrO_2@BCNT catalyst after HER. This will generate a partially reduced IrO_2 nanoparticle, namely IrO_x, covered with H atoms. We examined the HER activity of this nanoparticle by adding one additional H atom to various different sites on the surface. We found that the H atom added to the Ir atom at the tip of the IrO_x nanoparticle has nearly perfect adsorption energy leading to HER overpotential as low as 0.05 V as shown in Fig. 6, which is even lower than that on Pt(1 1 1) surface (0.07 V). The reduced IrO_2 nanoparticle

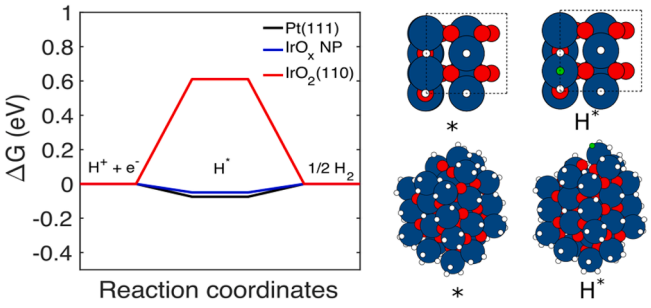

Fig. 6. Free energy diagrams for HER on Pt(1 1 1), IrO_2(1 1 0), and IrO_x nanoparticle. The atomic structures of adsorbed H* on O-deficient IrO_2(1 1 0) and IrO_x nanoparticle are shown. The adsorbed H* is colored light green.

dramatically outperforms the reduced IrO_2 surface because the nanoparticle can be reduced to a state that is more metallic, which enhances H binding. In our H-covered IrO_x model, the O:Ir ratio is close to 1:1. Consequently, the Ir atoms located at the tip of the nanoparticle only binds to 2–3O atoms, which makes them retaining more electrons from bonding with O ligands. And hence, the reduced Ir atoms can share more electrons with H*, and thus enhance the H binding. The Bader analysis shows that the Ir atoms at the tip of the nanoparticle have about 8 electrons and it is about 0.6 more electron than the Ir atom on the reduced IrO_2 (1 1 0) surface. For comparison, the metallic Ir in Ir fcc metal has about 9 electrons. Since the pure IrO_2 shows poor HER activity, the B-doped CNT plays a key role for accelerating electron transfer to partially reduce the surface Ir species. Thus, the efficient active sites for HER on the IrO_2@BCNT catalyst should be the partially reduced IrO_x nanoparticles.

4. Conclusions

In summary, we reported a high-performance bifunctional IrO_2@BCNT catalyst fabricated by supporting ultrafine iridium species on boron-doped carbon nanotubes. The iridium loadings would influence the electrocatalytic activities. On the 3%IrO_2@BCNT, to deliver a current density of 10 mA cm^{-2}, the HER overpotential is 26, 56, and 61 mV, while the OER overpotential is 291, 241, and 382 mV in 0.5 M H_2SO_4, 1 M KOH, and 1 M PBS, respectively. Moreover, 3%IrO_2@BCNT can be used as both anode and cathode electrocatalysts for overall water splitting with ultra-low potentials of 1.517, 1.513, and 1.591 V vs RHE to reach a current density of 10 mA cm^{-2} in 0.5 M H_2SO_4, 1.0 M KOH, and 1 M PBS, respectively. Theoretical calculations revealed that over-oxidized and significantly reduced ultrafine IrO_2 nanoparticles are responsible for the observed excellent OER and HER activities, respectively.

Declaration of Competing Interest

The authors declare that they have no known competing financial interests or personal relationships that could have appeared to influence the work reported in this paper.

Acknowledgments

This work was supported by the National Natural Science Foundation of China (22075099), Natural Science Foundation of Jilin Province (20180101291JC).

Appendix A. Supplementary data

Supplementary data to this article can be found online at https://doi.org/10.1016/j.cej.2021.129567.

References

[1] Y. Li, Y. Sun, Y. Qin, W. Zhang, L. Wang, M. Luo, H. Yang, S. Guo, Recent advances on water-splitting electrocatalysis mediated by noble-metal-based nanostructured materials, Adv. Energy Mater. 10 (2020) 1903120.
[2] X. Wen, J. Guan, Recent progress on MOF-derived electrocatalysts for hydrogen evolution reaction, Appl. Mater. Today 16 (2019) 146–168.
[3] Q. Zhang, J. Guan, Single-atom catalysts for electrocatalytic applications, Adv. Funct. Mater. 30 (2020) 2000768.
[4] Q. Zhang, J. Guan, Atomically dispersed catalysts for hydrogen/oxygen evolution reactions and overall water splitting, J. Power Sour. 471 (2020), 228446.
[5] Y. Zhao, N. Jia, X.-R. Wu, F.-M. Li, P. Chen, P.-J. Jin, S. Yin, Y. Chen, Rhodium phosphide ultrathin nanosheets for hydrazine oxidation boosted electrochemical water splitting, Appl. Catal. B 270 (2020), 118880.
[6] G. Ma, Q. Xue, J. Zhu, X. Zhang, X. Wang, H. Yao, G. Zhou, Y. Chen, Ultrafine Rh nanocrystals decorated ultrathin NiO nanosheets for urea electro-oxidation, Appl. Catal. B 265 (2020), 118567.
[7] H. Sun, Z. Yan, F. Liu, W. Xu, F. Cheng, J. Chen, Self-supported transition-metal-based electrocatalysts for hydrogen and oxygen evolution, Adv. Mater. 32 (2020) 1806326.
[8] C. Zhu, Z. Yin, W. Lai, Y. Sun, L. Liu, X. Zhang, Y. Chen, S.-L. Chou, Fe-Ni-Mo nitride porous nanotubes for full water splitting and Zn-air batteries, Adv. Energy Mater. 8 (2018) 1802327.
[9] Y. Yu, J. Zhou, Z. Sun, Novel 2D transition-metal carbides: ultrahigh performance electrocatalysts for overall water splitting and oxygen reduction, Adv. Funct. Mater. 2000570 (2020).
[10] Y. Lian, H. Sun, X. Wang, P. Qi, Q. Mu, Y. Chen, J. Ye, X. Zhao, Z. Deng, Y. Peng, Carved nanoframes of cobalt-iron bimetal phosphide as a bifunctional electrocatalyst for efficient overall water splitting, Chem. Sci. 10 (2019) 464–474.
[11] Y. Liu, S. Jiang, S. Li, L. Zhou, Z. Li, J. Li, M. Shao, Interface engineering of (Ni, Fe) S2@MoS2 heterostructures for synergetic electrochemical water splitting, Appl. Catal. B 247 (2019) 107–114.
[12] A. Chunduri, S. Gupta, O. Bapat, A. Bhide, R. Fernandes, M.K. Patel, V. Bambole, A. Miotello, N. Patel, A unique amorphous cobalt-phosphide-boride bifunctional electrocatalyst for enhanced alkaline water-splitting, Appl. Catal. B 259 (2019), 118051.
[13] F.-S. Zhang, J.-W. Wang, J. Luo, R.-R. Liu, Z.-M. Zhang, C.-T. He, T.-B. Lu, Extraction of nickel from NiFe-LDH into Ni2P@NiFe hydroxide as a bifunctional electrocatalyst for efficient overall water splitting, Chem. Sci. 9 (2018) 1375–1384.
[14] Z. Xiao, Y. Wang, Y.-C. Huang, Z. Wei, C.-L. Dong, J. Ma, S. Shen, Y. Li, S. Wang, Filling the oxygen vacancies in Co3O4 with phosphorus: an ultra-efficient electrocatalyst for overall water splitting, Energy Environ. Sci. 10 (2017) 2563–2569.
[15] F. Shen, Y. Wang, G. Qian, W. Chen, W. Jiang, L. Luo, S. Yin, Bimetallic iron-iridium alloy nanoparticles supported on nickel foam as highly efficient and stable catalyst for overall water splitting at large current density, Appl. Catal. B 278 (2020), 119327.
[16] P. Salimi, M.M. Najafpour, A simple method for synthesizing highly active amorphous iridium oxide for oxygen evolution under acidic conditions, Chem. Eur. J. 26 (2020) 17063–17068.
[17] J. Du, J. Quinson, D. Zhang, F. Bizzotto, A. Zana, M. Arenz, Bifunctional Pt-IrO2 catalysts for the oxygen evolution and oxygen reduction reactions: alloy nanoparticles versus nanocomposite catalysts, ACS Catal. 11 (2021) 820–828.
[18] X. Zou, Y. Zhang, Noble metal-free hydrogen evolution catalysts for water splitting, Chem. Soc. Rev. 44 (2015) 5148–5180.
[19] X. Liang, L. Shi, R. Cao, G. Wan, W. Yan, H. Chen, Y. Liu, X. Zou, Perovskite-type solid solution nano-electrocatalysts enable simultaneously enhanced activity and stability for oxygen evolution, Adv. Mater. 32 (2020) 2001430.
[20] C. Van Pham, M. Buehler, J. Knoeppel, M. Bierling, D. Seeberger, D. Escalera-Lopez, K.J.J. Mayrhofer, S. Cherevko, S. Thiele, IrO2 coated TiO2 core-shell microparticles advance performance of low loading proton exchange membrane water electrolyzers, Appl. Catal. B 269 (2020), 118762.
[21] J.R. Esquius, D.J. Morgan, I. Spanos, D.G. Hewes, S.J. Freakley, G.J. Hutchings, Effect of base on the facile hydrothermal preparation of highly active IrOx oxygen evolution catalysts, ACS Appl. Energy Mater. 3 (2020) 800–809.
[22] T. Nishimoto, T. Shinagawa, T. Naito, K. Takanabe, Microkinetic assessment of electrocatalytic oxygen evolution reaction over iridium oxide in unbuffered conditions, J. Catal. 391 (2020) 435–445.
[23] V. Pfeifer, T.E. Jones, J.J.V. Velez, R. Arrigo, S. Piccinin, M. Haevecker, A. Knop-Gericke, R. Schloegl, In situ observation of reactive oxygen species forming on oxygen-evolving iridium surfaces, Chem. Sci. 8 (2017) 2143–2149.
[24] F. Li, G.-F. Han, H.-J. Noh, J.-P. Jeon, I. Ahmad, S. Chen, C. Yang, Y. Bu, Z. Fu, Y. Lu, J.-B. Baek, Balancing hydrogen adsorption/desorption by orbital modulation for efficient hydrogen evolution catalysis, Nat. Commun. 10 (2019) 4060.
[25] P. Jiang, J. Chen, C. Wang, K. Yang, S. Gong, S. Liu, Z. Lin, M. Li, G. Xia, Y. Yang, J. Su, Q. Chen, Tuning the activity of carbon for electrocatalytic hydrogen evolution via an iridium-cobalt alloy core encapsulated in nitrogen-doped carbon cages, Adv. Mater. 30 (2018) 1705324.
[26] W.-H. Lai, L.-F. Zhang, W.-B. Hua, S. Indris, Z.-C. Yan, Z. Hu, B. Zhang, Y. Liu, L. Wang, M. Liu, R. Liu, Y.-X. Wang, J.-Z. Wang, Z. Hu, H.-K. Liu, S.-L. Chou, S.-X. Dou, General π-electron-assisted strategy for Ir, Pt, Ru, Pd, Fe, Ni single-atom electrocatalysts with bifunctional active sites for highly efficient water splitting, Angew. Chem. Int. Ed. 58 (2019) 11868–11873.
[27] Q. Zhang, Z. Duan, Y. Wang, L. Li, B. Nan, J. Guan, Atomically dispersed iridium catalysts for multifunctional electrocatalysis, J. Mater. Chem. A (2020), https://doi.org/10.1039/d1030ta05750a.
[28] L. Li, B. Wang, G. Zhang, G. Yang, T. Yang, S. Yang, S. Yang, Electrochemically modifying the electronic structure of IrO(2)nanoparticles for overall electrochemical water splitting with extensive adaptability, Adv. Energy Mater. 10 (2020) 2001600.
[29] J. Du, S. Li, Z. Du, S. Meng, B. Li, Boron/oxygen-codoped graphitic carbon nitride nanomesh for efficient photocatalytic hydrogen evolution, Chem. Eng. J. 407 (2021), 127114.
[30] J. Yin, J. Jin, M. Lu, B. Huang, H. Zhang, Y. Peng, P. Xi, C.-H. Yan, Iridium single atoms coupling with oxygen vacancies boosts oxygen evolution reaction in acid media, J. Am. Chem. Soc. 142 (2020) 18378–18386.
[31] Q. Wang, X. Huang, Z.L. Zhao, M. Wang, B. Xiang, J. Li, Z. Feng, H. Xu, M. Gu, Ultrahigh-loading of Ir single atoms on NiO matrix to dramatically enhance oxygen evolution reaction, J. Am. Chem. Soc. 142 (2020) 7425–7433.
[32] F. Luo, H. Hu, X. Zhao, Z. Yang, Q. Zhang, J. Xu, T. Kaneko, Y. Yoshida, C. Zhu, W. Cai, Robust and stable acidic overall water splitting on Ir single atoms, Nano Lett. 20 (2020) 2120–2128.
[33] H. Kim, J. Kim, J. Kim, G.H. Han, W. Guo, S. Hong, H.S. Park, H.W. Jang, S.Y. Kim, S.H. Ahn, Dendritic gold-supported iridium/iridium oxide ultra-low loading electrodes for high-performance proton exchange membrane water electrolyzer, Appl. Catal. B 283 (2021), 119596.

[34] F. Luo, L. Guo, Y. Xie, J. Xu, K. Qu, Z. Yang, Iridium nanorods as a robust and stable bifunctional electrocatalyst for pH-universal water splitting, Appl. Catal., B 279 (2020), 119394.
[35] E. Perez, N.M. Carretero, S. Sandoval, A. Fuertes, G. Tobias, N. Casan-Pastor, Nitrographene oxide in iridium oxide hybrids: electrochemical modulation of N-graphene redox states and charge capacities, Mater. Chem. Front. 4 (2020) 1421–1433.
[36] X. Wu, B. Feng, W. Li, Y. Niu, Y. Yu, S. Lu, C. Zhong, P. Liu, Z. Tian, L. Chen, W. Hu, C.M. Li, Metal-support interaction boosted electrocatalysis of ultrasmall iridium nanoparticles supported on nitrogen doped graphene for highly efficient water electrolysis in acidic and alkaline media, Nano Energy 62 (2019) 117–126.
[37] A. Zagalskaya, V. Alexandrov, Mechanistic Study of IrO2 Dissolution during the Electrocatalytic Oxygen Evolution Reaction, J. Phys. Chem. Lett. 11 (2020) 2695–2700.
[38] D.F. Abbott, D. Lebedev, K. Waltar, M. Povia, M. Nachtegaal, E. Fabbri, C. Coperet, T.J. Schmidt, Iridium oxide for the oxygen evolution reaction: correlation between particle size, morphology, and the surface hydroxo layer from operando XAS, Chem. Mater. 28 (2016) 6591–6604.
[39] W.-H. Lai, L.-F. Zhang, W.-B. Hua, S. Indris, Z.-C. Yan, Z. Hu, B. Zhang, Y. Liu, L. Wang, M. Liu, R. Liu, Y.-X. Wang, J.-Z. Wang, Z. Hu, H.-K. Liu, S.-L. Chou, S.-X. Dou, General pi-Electron-Assisted Strategy for Ir, Pt, Ru, Pd, Fe, Ni Single-Atom Electrocatalysts with Bifunctional Active Sites for Highly Efficient Water Splitting, Angew. Chem., Int. Ed., 58 (2019) 11868-11873.
[40] Z.-H. Sheng, H.-L. Gao, W.-J. Bao, F.-B. Wang, X.-H. Xia, Synthesis of boron doped graphene for oxygen reduction reaction in fuel cells, J. Mater. Chem. 22 (2012) 390–395.
[41] F. Nattino, N. Marzari, Operando XANES from first-principles and its application to iridium oxide, Phys. Chem. Chem. Phys. 22 (2020) 10807–10818.
[42] A.R. Hillman, M.A. Skopek, S.J. Gurman, X-Ray spectroscopy of electrochemically deposited iridium oxide films: detection of multiple sites through structural disorder, Phys. Chem. Chem. Phys. 13 (2011) 5252–5263.
[43] H.G.S. Casalongue, M.L. Ng, S. Kaya, D. Friebel, H. Ogasawara, A. Nilsson, In situ observation of surface species on iridium oxide nanoparticles during the oxygen evolution reaction, Angew. Chem. Int. Ed. 53 (2014) 7169–7172.
[44] J. Guan, X. Wen, Q. Zhang, Z. Duan, Atomic rhodium catalysts for hydrogen evolution and oxygen reduction reactions, Carbon 164 (2020) 121–128.
[45] L. Cao, Q. Luo, W. Liu, Y. Lin, X. Liu, Y. Cao, W. Zhang, Y. Wu, J. Yang, T. Yao, S. Wei, Identification of single-atom active sites in carbon-based cobalt catalysts during electrocatalytic hydrogen evolution, Nat. Catal. 2 (2019) 134–141.
[46] M.S. Burke, M.G. Kast, L. Trotochaud, A.M. Smith, S.W. Boettcher, Cobalt-iron (Oxy)hydroxide oxygen evolution electrocatalysts: the role of structure and composition on activity, stability, and mechanism, J. Am. Chem. Soc. 137 (2015) 3638–3648.
[47] F.G. Sen, A. Kinaci, B. Narayanan, S.K. Gray, M.J. Davis, S.K.R. S. Sankaranarayanan, M.K.Y. Chan, Towards accurate prediction of catalytic activity in IrO2 nanoclusters via first principles-based variable charge force field, J. Mater. Chem. A 3 (2015) 18970–18982.